AGU PUBLICATIONS

JGR

Journal of Geophysical Research: Solid Earth

RESEARCH ARTICLE
10.1002/2015JB012448

Key Points:
- In situ fault surface measured
- Numerical model made directly from point cloud
- Earthquake rupture recreated on model fault

Correspondence to:
T. Parsons,
tparsons@usgs.gov

Citation:
Parsons, T., and D. L. Minasian (2015), Earthquake rupture process recreated from a natural fault surface, *J. Geophys. Res. Solid Earth*, *120*, 7852–7862, doi:10.1002/2015JB012448.

Received 13 AUG 2015
Accepted 23 OCT 2015
Accepted article online 27 OCT 2015
Published online 27 NOV 2015

Earthquake rupture process recreated from a natural fault surface

Tom Parsons[1] **and Diane L. Minasian**[1]

[1]U.S. Geological Survey, Menlo Park, California, USA

Abstract What exactly happens on the rupture surface as an earthquake nucleates, spreads, and stops? We cannot observe this directly, and models depend on assumptions about physical conditions and geometry at depth. We thus measure a natural fault surface and use its 3-D coordinates to construct a replica at 0.1 m resolution to obviate geometry uncertainty. We can recreate stick-slip behavior on the resulting finite element model that depends solely on observed fault geometry. We clamp the fault together and apply steady state tectonic stress until seismic slip initiates and terminates. Our recreated $M \sim 1$ earthquake initiates at contact points where there are steep surface gradients because infinitesimal lateral displacements reduce clamping stress most efficiently there. Unclamping enables accelerating slip to spread across the surface, but the fault soon jams up because its uneven, anisotropic shape begins to juxtapose new high-relief sticking points. These contacts would ultimately need to be sheared off or strongly deformed before another similar earthquake could occur. Our model shows that an important role is played by fault-wall geometry, although we do not include effects of varying fluid pressure or exotic rheologies on the fault surfaces. We extrapolate our results to large fault systems using observed self-similarity properties and suggest that larger ruptures might begin and end in a similar way, although the scale of geometrical variation in fault shape that can arrest a rupture necessarily scales with magnitude. In other words, fault segmentation may be a magnitude-dependent phenomenon and could vary with each subsequent rupture.

1. Introduction

Important questions about the earthquake rupture process remain unanswered, complicating our ability to forecast them [e.g., *Field et al.*, 2014]. There is some apparent predictability regarding where earthquakes begin and end [e.g., *Wesnousky*, 2006], but uncertainties are large enough that hazard studies do not necessarily assume that earthquakes will repeat themselves within segment boundaries [*Field and Page*, 2011]. In fact, debate persists whether individual faults host repeated characteristic magnitude earthquakes or follow a power law distribution [e.g., *Schwartz and Coppersmith*, 1984; *Wesnousky*, 1994; *Stein and Newman*, 2004; *Page et al.*, 2011; *Page and Felzer*, 2015]. Here we recreate a fault and its earthquakes numerically, with a model taken directly from a natural surface (Figure 1), so that we can explore the consequences of its shape and gain direct insight into earthquake initiation and arrest.

We measure an exposed fault with ground-based lidar and use the 3-D point cloud to build a finite element replica (Figure 2). This model naturally exhibits stick-slip behavior when stress is applied in its rake direction, behavior that is difficult to capture numerically using randomized elastic surfaces, although successful results have been achieved with discrete element models [e.g., *Fournier and Morgan*, 2012]. In the context of our model, we define stick slip as the fault resisting applied stress (sticking) as it begins a nucleation process (infinitesimal slip), until finally, significant displacement occurs at relatively high velocity (slipping). We cannot, at this stage, conduct a fully dynamic rupture simulation while simultaneously incorporating the full complexity of a natural fault surface because of computational limitations. Instead, rupture evolution is approximated by very short time steps that are solved statically. In this way we can observe quasi-dynamic features such as relative slip speed and the spatial distribution of preseismic slip that occur as a consequence of fault geometry. Our calculations are performed in the elastic limit, and no plastic yield is modeled, which is the main limitation at small scales and for the largest earthquakes. If we accept this simulation as a reasonable approximation of the natural process, then we discover which features of the fault surface encourage initiation of earthquake slip, those that act to arrest it, and the influence of fault roughness on asperities. Earthquake faults are known to exhibit self-similarity and scale invariant complexity, which contextualizes our results to larger, and thus dangerous fault zones.

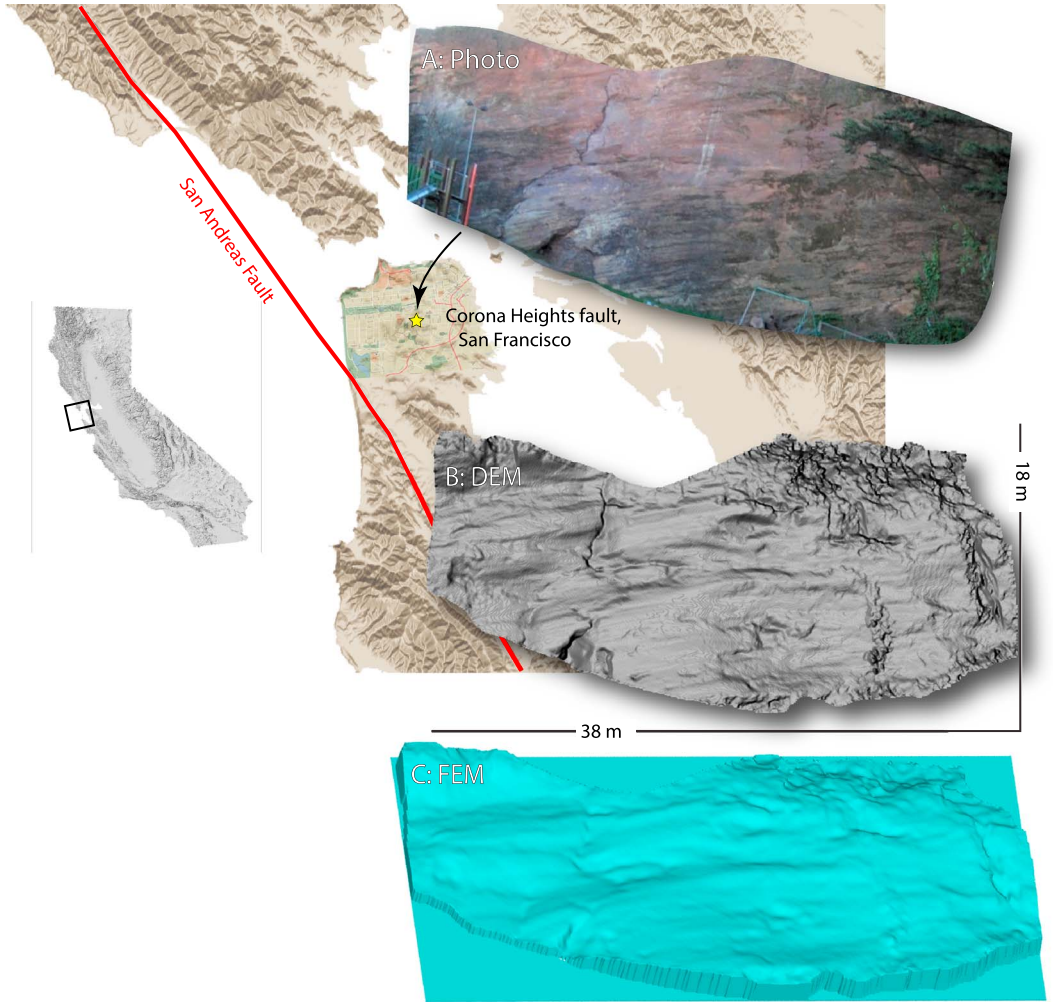

Figure 1. The yellow star shows the location of the Corona Heights fault in the city of San Francisco, CA, USA. (a) A photo of the Corona Heights fault surface that was scanned with ground-based lidar. (b) The resulting point cloud was used to make a 0.1 m spaced digital elevation model (DEM) that defined node locations of the (c) finite element model (see also Figure 2).

We recognize that a natural fault in situ is a far more complex system than we can replicate numerically at this time. However, we can experiment to see what happens when a numerical representation of a natural fault is subjected to applied stress. This approach can allow an assessment of the potential role of surface heterogeneity on slip propagation and nucleation.

2. Observations

The Corona Heights fault is located within the city of San Francisco, CA (Figure 1), and it cuts through an early Jurassic [*Murchey and Jones*, 1984], massive radiolarian chert unit of the Franciscan Formation [*Schlocker*, 1974]. The timing of faulting on the dextral [*Kirkpatrick et al*., 2013] Corona Heights fault is undetermined, but we know that it was exposed during quarrying operations by George and Harry Gray that began in 1909 and ceased shortly after the murder of George Gray in 1914 over a refusal to pay back wages [*Bevk*, 2013]. The fault thus has well-preserved corrugation and slickenside features, making it ideal for detailed study [*Candela et al*., 2011, 2012; *Kirkpatrick et al.,* 2013; *Kirkpatrick and Brodsky*, 2014]. The Corona Heights fault offset is estimated to be ~50 m or less [*Kirkpatrick and Brodsky*, 2014]. Natural fault surfaces tend to have anisotropic roughness [*Brown and Scholz*, 1985; *Power et al.,* 1987], which is true in the case of the Corona Heights fault [*Kirkpatrick and Brodsky*, 2014].

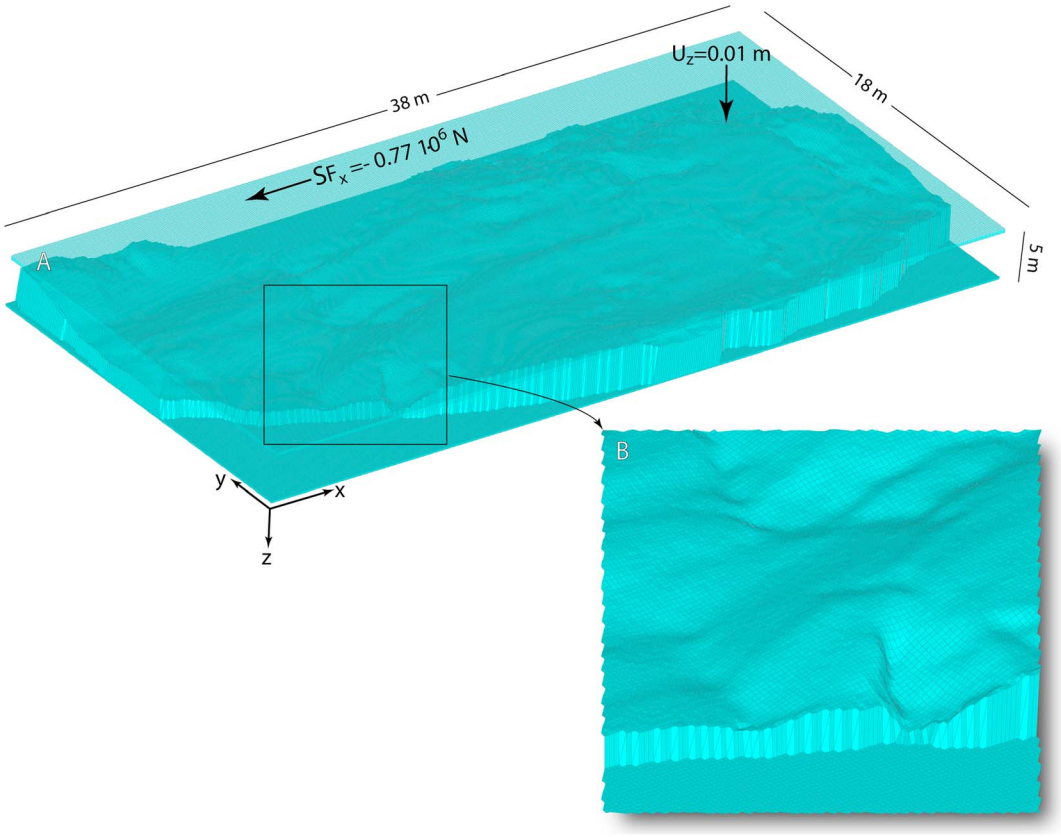

Figure 2. Finite element model showing the applied displacements/forces. The 2.5 m thick upper plate is made transparent so that its inverse, a 2.5 m thick lower plate, and the fault surface can be seen. The model is clamped by moving the upper plate down by 0.01 m. Fault surface slip was caused by fixing the lower plate base and applying a ramped force on the upper plate in the $-x$ direction. No lateral slip was imposed, only stress. In Figure 2b a close-up view of the fault surface mesh is shown to illustrate the resolution (0.1 m node spacing).

We use a tripod mounted Riegl Z210 laser scanner system (lidar) to develop a 3-D model of the Corona Heights fault. Multiple scans are collected to fill in locations not directly in the line of sight of the laser and to expand the range and density of the point data. Data are collected at a rate of 8000 points per second, scanning a range of 336° in the horizontal direction and 40° from the horizontal in the vertical direction. We conduct scans over a range from 1 mm to 10 cm resolution. Processing is performed using I-SiTE software specifically designed to handle laser scan data. Point data are filtered to remove extraneous laser returns from the point clouds. Points reflected from vegetation are manually cropped from each of the clouds, and topographic filters that select the lowest level in the point clouds are also used to remove vegetation.

We use full-resolution processed lidar points to construct a regularly spaced digital elevation model (DEM) (Figure 1). We perform a grid search to find the horizontal plane that minimizes long-wavelength relief on the fault surface and rotate the coordinate system so that plane is horizontal. The original orientation of the fault when it was active is unknown, but it has a right-lateral rake; we rotate the DEM model so that the *x* direction is parallel to the observed slip direction as interpreted from striations (27° rotation counterclockwise about our *z* axis) [*Kirkpatrick and Brodsky*, 2014].

3. Model Development

The primary goal of our modeling is to assess the role that fault geometry/topography plays in generating and resisting earthquakes. The advantage of replicating a real fault surface in 3-D means that no geometrical assumptions are made for scales equal to or above the model node spacing. However, a number of tradeoffs also need to be made because a 3-D finite element model of a natural surface requires a very large number of

element nodes that have complex contact interactions. Therefore, as described below, a fully dynamic solution or one that includes exotic friction and mobile pore fluids remains outside our computational resources.

We subsample the DEM generated from lidar measurements to a 0.1 m spaced grid, which represents the minimum node spacing that can reasonably be meshed into a finite element model under our computer memory constraints. All calculations are made with the commercial ANSYS© software that enables large deformation (finite strain), although we treat rocks as elastic materials here to limit the number of parameters required. We begin with a meshed, initially rectangular prism (length 38 m, height 18 m, depth 2.5 m), and then move surface nodes to positions described by the DEM to recreate the fault surface. The inverse is done to another prism to create the upper plate (also 2.5 m thick) so that they fit together exactly (Figure 2). Where two sides of an actual fault are observed in detail, they mirror each other at lateral dimensions greater than 0.02 m [*Power and Tullis*, 1992], which is well below our 0.1 m spacing.

Both fault faces are draped with zero-thickness contact elements that obey a Coulomb failure criterion; we tested uniform friction coefficients ranging from $\mu = 0.2$ to $\mu = 0.8$. We fixed Poisson's ratio to 0.25 for all experiments. The total fault area in the model is 563.6 m^2. The model has 313,832 elastic elements characterized by a soft Young's modulus of $E = 5$ GPa; fault zones are expected to have reduced Young's moduli because of crushing and fracturing [*Gudmundsson*, 2004], with the approximate value of clays and other cohesive/plastic materials [*Kezdi*, 1974]. As a linear constant, the absolute value of Young's modulus is only important in terms of relating elastic strain (ε) to stress (σ) as $\varepsilon = \sigma/E$, but stress in our model comes from an applied steady state force. In other words, a higher Young's modulus results in the same behavior but at higher stress levels.

We generate stick-slip behavior by compressing the fault together ($uz = 0.01$ m) to create fault-normal (clamping) stress, which when combined with friction, acts to resist fault slip according to the Coulomb failure criterion $CFF \equiv |\bar{\tau}_f| + \mu(\sigma_n - p)$, where $\bar{\tau}_f$ is shear stress in the rake direction, σ_n is the stress normal to the fault plane, and p is pore fluid pressure (not explicitly modeled in this study). Sensitivity of failure to clamping can be assessed by the coefficient of friction (μ) or normal stress; we vary friction coefficient rather than uz displacement to avoid unduly affecting the shape of the fault surface before slip can occur. Changing the friction coefficient can account for pore fluid pressure variation in a rudimentary way if fluids are confined within the fault, or in fault parallel cracks that are pressurized uniformly by normal stresses [e.g., *Rice*, 1992; *Scholz*, 2002]. Given the significant topography of our modeled fault surface, we recognize that the role of pore fluids is necessarily simplified by our model. Finally, we assume that the far-field stress state at the model boundaries does not vary over the spatial scale of the model (38 m by 18 m).

The model lower plate is fixed in all directions, and the model upper plate is loaded in the $-x$ direction to encourage dextral slip on the fault surface; a linear time-ramped force is applied across the entire top surface of the model from zero until the earthquake is completed. The maximum stress reached is $0.77 \cdot 10^6$ N applied on a unit area, which sums to 77.0 MPa of applied stress to the system; this is the stress applied to the model exterior, which has a slightly greater area than the embedded fault interface (Figure 2). This threshold depends linearly on the values of Young's modulus and the coefficient of friction and simply increases as they do. Model results are shown with relatively low values of $\mu = 0.2$ and $E = 5.0$ GPa. The fault mostly resists slipping prior to the maximum stress threshold, and then breaks free, generating a small earthquake. Force is accumulated at a uniform rate throughout the simulation, replicating steady state tectonic stressing.

In other words, loading is simulating tectonic stress with shear applied on one exterior face of the model, parallel to the fault slip direction, while the opposing face is held fixed (Figure 2). Stress is ramped up with time as we expect it to in the real Earth. We also apply a small component of fault-normal compression to hold the fault together. Application of stress does not result in immediate, significant slip on the fault because there are multiple points of contact that resist slip because of their geometry. Thus, elastic strain builds in the fault walls and at resisting points on the fault. Competing with those resisting contact points are other, releasing zones where slip is encouraged. As will be discussed, it appears in the model that earthquake initiation depends in part on the balance between sticking and sliding fault topography and the ability of releasing points to organize into large patches of slip that can overcome resisting geometry.

The modeling we conduct is static rather than fully dynamic. This has two primary effects: (1) there is no accounting for inertial influences on simulated earthquake rupture. In the real Earth, once the faulted mass

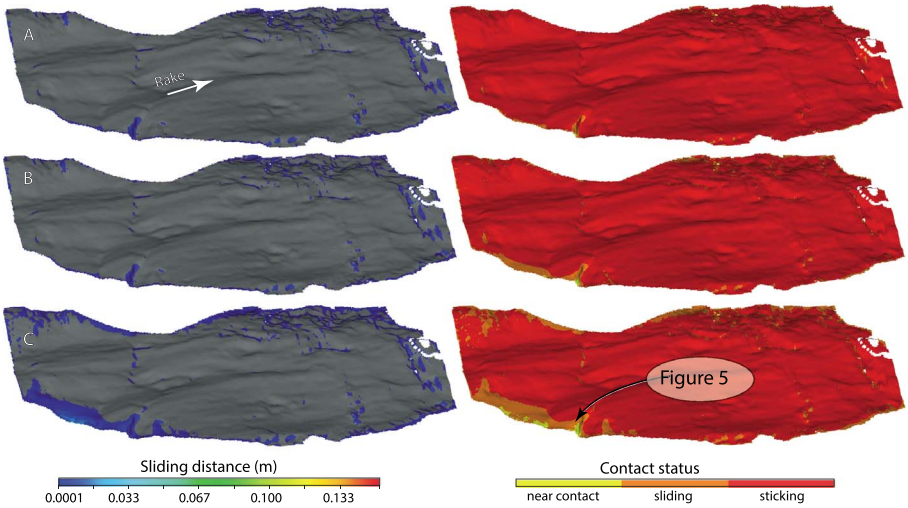

Figure 3. Recreated $M = 0.95$ earthquake on the Corona Heights fault. In steps (a–c) the prerupture phase is shown, where most of the fault surface is locked (red shading in adjacent column). Gray areas are regions with no slip (locked). Near contact means that contact elements are beginning to open up as a result of slip. Offset can still occur in these areas, but not as full frictional contact.

begins to move, it has momentum that must be damped for the earthquake to cease. In our case, rupture begins when the shear stress state exceeds resistance and ceases when the opposite is true. (2) We ramp the model forcing over time steps, but the time variable in our case only tracks the relative durations that the fault is in different stages of loading and slip. The absolute time scale is arbitrary and depends on the rate that we apply force. This means we cannot give rupture velocity or discuss rupture preparation times in absolute terms, but only over a normalized period. On the other hand, we have to estimate relatively few parameters as compared with fully dynamic simulations [e.g., *Duan and Oglesby*, 2005; *Xu et al.,* 2015], and those that we do need (friction coefficient, Young's modulus, force amplitude, and time step) all trade off

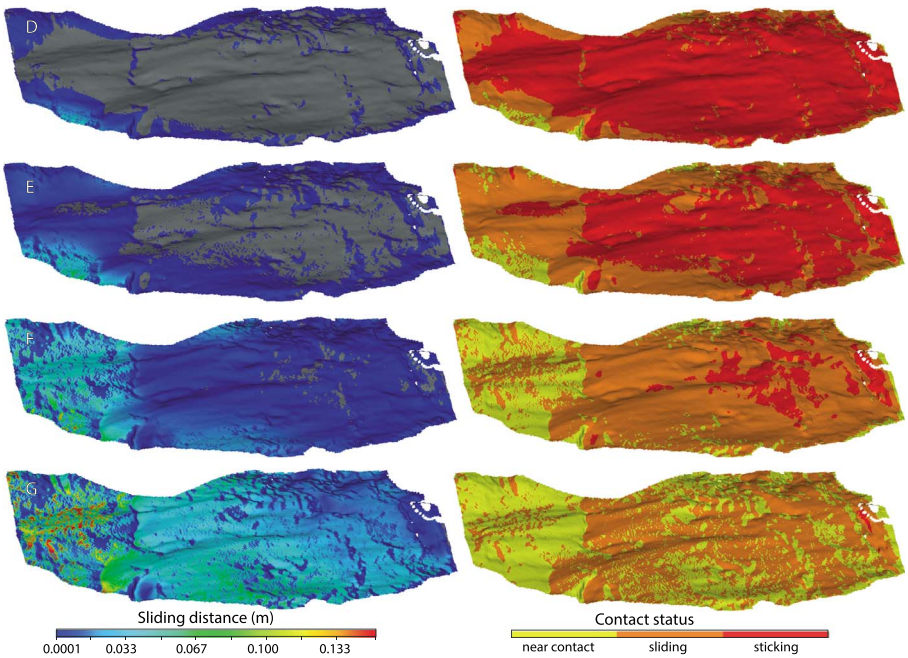

Figure 4. At step (d) low-magnitude slip begins around the fault edges and in areas of steep fault-surface topography (sliding areas are shaded orange in adjacent column). At steps (e–g) slip spreads in the rake direction, and areas with highest slip experience opening (yellow shading) with slip ceasing there.

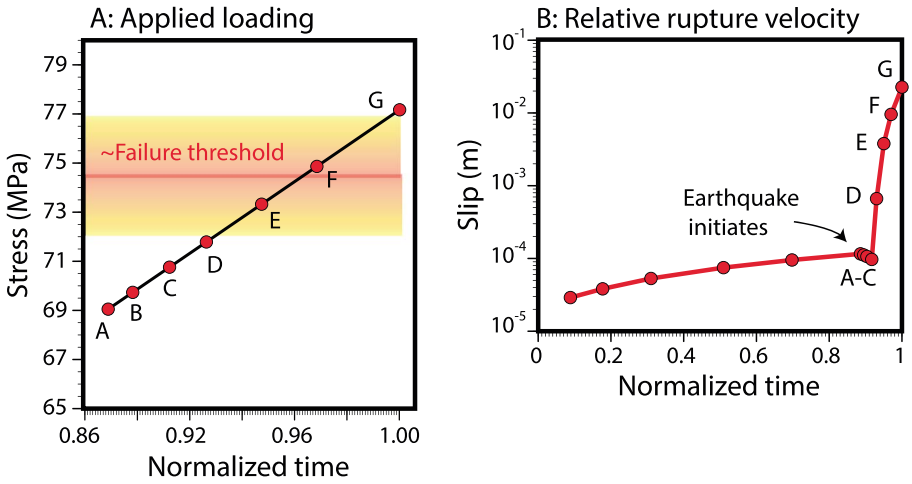

Figure 5. (a) Applied loading and approximate failure threshold range is plotted. The failure threshold is approximate because the onset of slip is gradual. Applied stress continues after failure; this is analogous to the plates not stopping after an earthquake. There is a stress drop on the fault that is spatially variable (Figure 6). (b) An example slip velocity plot is shown that is taken from the point indicated on the fault surface in Figure 3. Letters A–G correspond to stages shown in Figures 3 and 4. Time is normalized because the solution is static, but the relative time shows a strong acceleration that begins around stage C.

linearly. The primary contribution from our modeling is thus quantifying the role of fault topography on rupture resistance, initiation, and termination.

4. Model Results

By replicating a natural fault surface, we can generate small ($M \sim 1.0$), simulated earthquakes (Figures 3 and 4) without enforcing any special friction conditions to initiate or stop ruptures. Typically, a smooth frictional surface will slip/creep in direct proportion to applied forces in finite element models, and it is difficult to achieve spontaneous stick-sip behavior without predefining failure conditions [e.g., *Lynch and Richards*, 2001; *Xing et al.*, 2004; *Coon et al.*, 2011]. This is because it is a lower energy solution for a model fault to creep compared with distorting the entire model volume surrounding a locked fault.

We apply uniform compression across the natural fault and then begin steady state forcing in the rake direction to replicate tectonic stress accumulation (Figure 2) as frictional resistance is overcome. The fault slips very slowly as stress builds up and then accelerates rapidly during the final seismic stages (Figure 4). The areas that slip initially are small (on the order of a few square centimeters), and they slip less than 1 mm (Figure 3). Such small slips would likely not be detectable with seismographs. Most of the fault surface accumulates a small amount of slip (<1 mm) before more significant offset takes place.

In the model, the primary control on earthquake nucleation, growth, and cessation is the shape of the fault walls. Low-magnitude slip begins around areas of steep topography on the fault surface. Small lateral offsets quickly reduce clamping stress at these points if they are favorably oriented (Figure 3). Accelerating slip begins to spread across much of the fault plane (Figures 4 and 5) and propagates in the rake direction. This appears like a unilateral rupture that propagates across the fault plane in the slip direction. An alternative interpretation is that the earthquake consists of a cascade of slips of self-similar sizes [e.g., *Main*, 1996] that coalesce and propagate laterally. The distribution of high relief contact points where rupture initiates is asymmetrically distributed where seismic slip begins in the model, thus either interpretation is possible.

Most of the contact status evolves from "sliding" to "near contact" after relatively significant slip occurs (~3–5 cm). These designations are reported by the contact elements we use, with near contact defined as a contact-target pair that is beginning to separate. This happens because the fault faces are no longer perfectly matched after offset occurs. The largest slips therefore behave more like a pulse than a continuously slipping crack because most of the areas that have significant slip cause the fault to open up

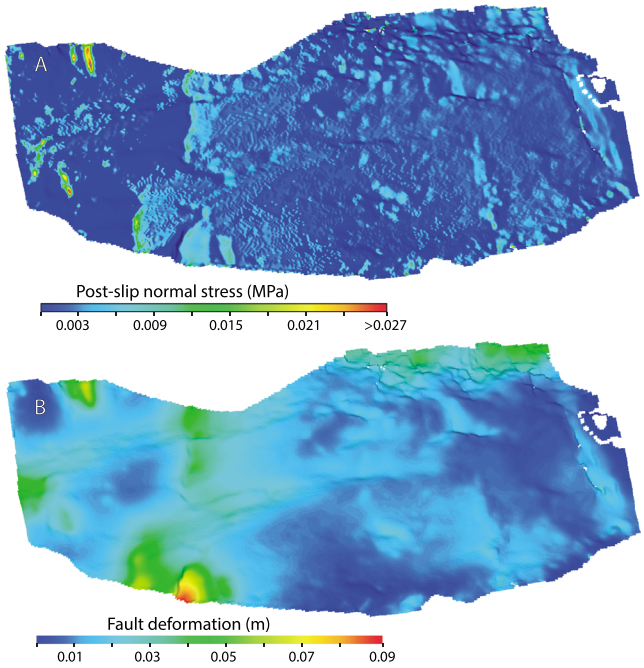

Figure 6. (a) Post-earthquake distribution of normal (clamping) stress. Slip on the rough fault surface causes stress concentrations at localized points along the fault, which are responsible for arresting slip in the model. (b) The fault surface deformation is shown, which corresponds to areas of stress concentration. These are areas that must change shape to enable further slip in subsequent earthquakes.

and lose contact; pulse-like ruptures are found to fit empirical earthquake scaling relations better than crack-like ones [e.g., *Noda et al*., 2009].

If we examine slip at a point on the fault surface over the duration of the model, we can see the relative time history of fault sip under a constant load (Figure 5). Over almost the entire load period the cumulative slip only grows from ~10^{-5} m to ~10^{-4} m. Once enough offset has occurred to unclamp a small contiguous area, slip begins to happen rapidly, approaching 10^{-1} m before the fault opens up and contact is lost. Slip then evolves into another part of the fault (Figure 4).

Most of the fault surface is able to reduce frictional stress by slipping, although isolated parts of the fault exhibit increased stress (Figure 6a). These are places where opposing steep fault surface gradients come into contact and build strong contact pressure with continued slip. Increased contact pressure translates into frictional resistance according to Coulomb failure theory (product of normal stress and friction coefficient). In some cases these contacts amount to collisions with virtually no ability to slip in a strike-slip sense. It follows that these points of contact are places of greatest fault-wall deformation in the model (Figure 6b), which is a strain response to the stress increase. Model elements become highly distorted and unstable as the earthquake ceases, indicating a need for fracture if the earthquake were to continue. These areas are thus the primary inhibitors to continued slip and must permanently deform before another similarly sized earthquake can happen in the model.

The input Coulomb friction coefficient of the fault material does not influence our results because the shape of the fault controls its slip behavior. We generate nearly the identical earthquake with a complete range of friction coefficients ($\mu = 0.2$–0.8); the only effect of the friction coefficient is a linear dependence on the time step that slip initiation begins. One interpretation is that the concept of friction at the fault zone scale has less to do with inherent material properties of the juxtaposed rocks than it does with the map-scale roughness of the fault; this has been noted experimentally [e.g., *Ben-David and Fineberg*, 2011; *Lockner and Byerlee*, 1993].

Our model does not include fault gouge, which has nonlinear rheology and reduced material friction relative to the brittle fault wall rocks [e.g., *Wibberley et al*., 2008; *Moore and Rymer*, 2007]. For the relatively small offset (~50 m or less [*Kirkpatrick and Brodsky*, 2014]) Corona Heights fault, this layer would likely have been thin and possibly not uniformly distributed [e.g., *Scholz*, 1987; *Sibson*, 2003]. However, the presence of a gouge layer could potentially affect the deformability of the fault zone through plastic strain during an earthquake, as well as influence rupture stability [e.g., *Marone and Kilgore*, 1993; *Marone*, 1995; *Marone et al*., 2009]. However, relief on the modeled section of the Corona Heights fault exceeds 1 m in places, which is an order of magnitude greater than typical gouge layers for a small offset fault [*Sibson*, 2003]. Also, the fact that the coefficient of friction in our models does not impact initiation or arrest of simulated earthquakes points to a potentially limited role for a gouge layer on our results. Gouge is more likely to affect seismic behavior on a smoother (relative to thickness), more mature (larger offset) fault surface [e.g., *Faulkner et al*., 2008; *Collettini et al*., 2009].

We calculate that the earthquake shown in Figure 3 has a magnitude $M = 0.95$, an average slip of 0.0307 m, a peak slip of 0.16 m, a moment release of $m_0 = 5.19 \cdot 10^{11}$ Nm, and a stress drop of 5.8 MPa. These values are within the range of observed microearthquakes [*Imanishi and Ellsworth*, 2006], although they depend on the physical properties we used to make the model (friction coefficient and Young's modulus). Modeled earthquake magnitude is not limited by available slip area, but rather by the amount of possible cumulative slip. We are only able to model a small fault area at detailed resolution; it is possible that if this fault were embedded within a larger surface where greater slip was taking place, then the geometric obstacles we encounter that arrest slip might be overcome, especially if inertial effects are accounted for.

5. Qualitative Consistency With Rate-State Friction

We note similarities between our models of fault slip to predictions from laboratory observations of rate and state friction [*Dieterich*, 1979, 1992]. In that conception, friction $\boldsymbol{\mu}(t)$ takes the form $\mu(t) = \mu^* + A\ln\frac{V}{V^*} + B\ln\frac{\theta V^*}{D_c}$, where the time-dependent variables are slip velocity V, and state θ, which is a characterization of fault contacts that can evolve with time or slip [*Ruina*, 1983]. Rapid, unstable slip (an earthquake) happens after the critical slip distance (D_c) is traversed. Rate and state theory captures a wide array of fault behaviors including velocity weakening, velocity strengthening, stable slip (creep), and unstable slip (earthquakes), depending on the balance of the rate and state terms and values of the constants. Our model does not encompass this range, but some unstable slip features are reminiscent.

In our model, the fault must begin to unlock by steeper contact faces unclamping. As some of these areas begin to move, they add stress to adjacent areas that also begin to slip very slowly, with some larger patches coalescing (Figure 3). The difference between unstable and stable slip in the model is governed by this coalescing process being held for some period. This in turn is controlled by the fault zone rheology; in our stiff, elastic fault zone we see unstable slip. If the fault zone were soft enough to deform under a lower stress state we might observe more stable slip (creep).

For almost 90% of the time that the model fault is loaded (Figure 5), the slip distribution looks just like Figure 3a. This transition could be viewed as the critical slip distance necessary to initiate accelerating seismic slip. Slip weakening then occurs during the pulse of unclamping that sweeps across the fault in the rake direction (Figure 4). That pulse is in turn followed by widespread opening of the fault, and new contact points forming that interfere with slip. In Figure 6b, fault zone deformation is shown, which can be thought of as state evolution and strengthening. With continued loading, these patches would be the most likely to grow with increased applied stress. Thus, the balance between locking and unlocking would repeat, ultimately leading to a new rupture.

While these analogies are qualitative, there may be some links from laboratory-scale observations to fault zone outcrop scale through self-similarity. In the following section we explore a conceptual extrapolation of our model results to map-scale fault zones.

6. Extrapolation of Model Results to Larger Faults

Form our modeling exercise it appears that an earthquake may begin by slipping very small areas by very small amounts (Figure 3). If we could model the fault at a more detailed scale, we would probably find that even smaller areas are involved in initiating an earthquake because the topography of faults scales on a linear power spectrum [*Brown and Scholz*, 1985; *Power et al*., 1987; *Aviles et al*., 1987; *Okubo and Aki*, 1987; *Kagan*, 1991; *Candela et al*., 2012; *Renard et al*., 2013] and is thus self-similar. Ideally, we would be able to model a much larger surface at such detail to see a broader magnitude spectrum, but the numerical challenges exceed our capability at present. However, we might imagine that the model we created could be scaled up in size, and that through self-similarity, can be used to speculate about higher magnitude earthquakes.

This can be demonstrated by comparing perhaps the tiniest fault in California (the Corona Heights fault) to the largest, the San Andreas fault. We compare the topography of the Corona Heights fault to the inferred topography of the San Andreas fault through its surface trace with spatial Fourier transformation (Figure 7). Comparing along-strike profiles of the small-offset Corona Heights fault (0.1 m sample interval) with the

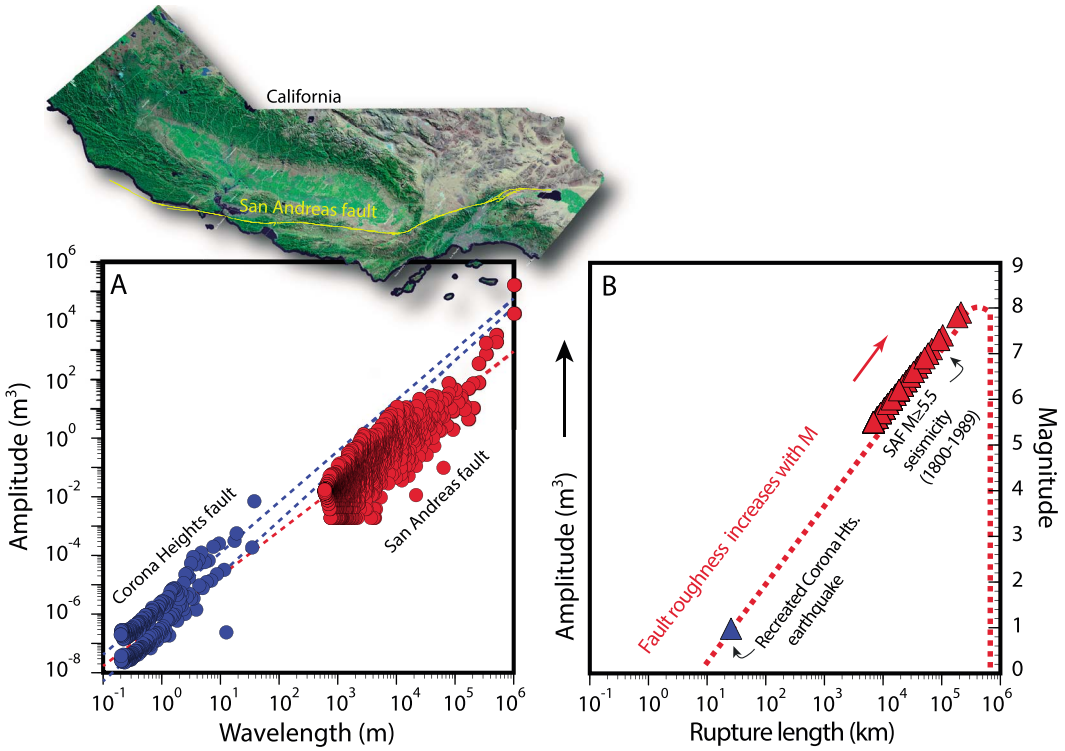

Figure 7. (a) Power spectral density of the Corona Heights and San Andreas faults showing the self-similarity of fault roughness at all scales; dashed blue lines show best power law fit to two profiles on the Corona Heights fault, and red dashed line to the San Andreas fault. (b) Earthquake magnitude, rupture length, and the amplitude of roughness are all correlated such that the scale of fault topography inhibiting ruptures is greater for higher magnitude earthquakes.

mapped trace [*Jennings*, 1994] of the mature San Andreas fault system (0.5 km sample interval) reveals a similar relationship between amplitude of fault topography versus wavelength for the two faults (Figure 7).

To compare the power spectra of different faults, we calculate sample spectral density, which is defined as $\widehat{F}(\omega_k) = nC_k^2$, where $C_k^2 = \frac{1}{n^2}\left|\sum_{x=1}^{n} f(x)e^{2\pi i(x-1)\omega_k}\right|^2$ for a set of sinusoidal amplitudes on a topographic profile $f(x)$ found at spatial frequencies $(1/n, 2/n, \ldots q/n)$, and $\omega_k = (k-1)/n$ is the set of natural frequencies for $k = 1, \ldots, \lfloor n/2 \rfloor + 1$, where $\lfloor\rfloor$ indicates the greatest integer function. Earthquake magnitudes on the San Andreas fault are taken from a historical compilation [*Toppozada et al.*, 2002], and their rupture lengths are calculated using an empirical relation [*Wells and Coppersmith*, 1994].

The San Andreas fault is capable of $M \sim 8$ and perhaps larger earthquakes [e.g., *Field et al.*, 2014], whereas our recreated Corona Heights fault earthquake has a maximum magnitude of $M \sim 1$ that is not controlled by its length, but rather its roughness. We show that for repeated slip to occur, these slip barriers must change shape, or be smoothed away. It is possible that the more mature San Andreas fault may lack the short wavelength features evidenced on the Corona Heights fault surface that we find inhibit significant slip and might have a minimum magnitude [e.g., *Aki*, 1987] as well as a maximum magnitude (Figure 7b). Such a process was interpreted from measured rougher fault surfaces for smaller offset faults than those with greater slip [*Sagy et al.*, 2007; *Childs et al.*, 2009]. However, if self-similarity persists to all scales [*Brown and Scholz*, 1985; *Power et al.*, 1987; *Aviles et al.*, 1987; *Okubo and Aki*, 1987; *Kagan*, 1991; *Candela et al.*, 2012; *Renard et al.*, 2013], then as some barriers are smoothed, others might be created. Thus, the scale of fault topography that inhibits slip may simply scale with magnitude and maximum slip. A long fault with a major asperity may develop enough energy after breaking to overcome smaller wavelength features. In such a case, the prediction is magnitude-dependent fault segmentation, such that a step-over or bend might stop a small rupture, but not a larger one. Also, since each rupture may generate a new set of contacts and rupture barriers (as in our model), then subsequent earthquake magnitudes might vary along the same fault length.

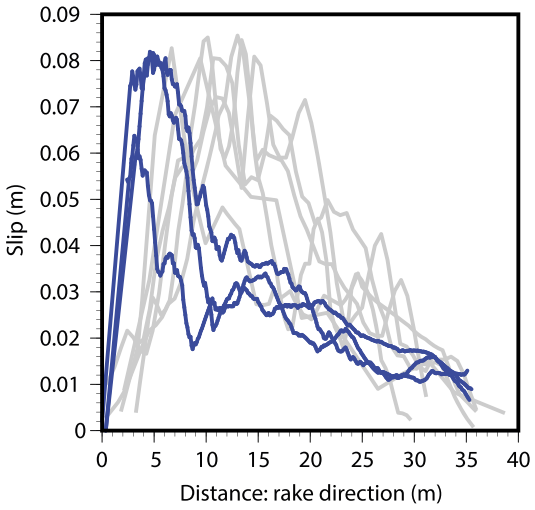

Figure 8. Blue lines show example slip versus distance profiles as modeled along the Corona Heights fault (axis labels refer to these lines). Gray lines show normalized examples from *Manighetti et al.* [2005] from measured surface slip along strike of global $M = 6.3$–$M = 7.7$ earthquakes. The purpose of this figure is to show that simulated and observed earthquakes have comparable, asymmetric slip distributions.

Additionally, not only are faults self-similar but the earthquakes that occur on them are shown to have self-similar slip distributions. *Manighetti et al.* [2005] examined more than 100 global earthquake slip distributions and found that they are asymmetric, being dominated by one region of strong slip followed by a long-tailed gradient that they describe as triangular in shape (Figure 8). They demonstrate that the high-slip patches (asperities) occupy approximately one third of the slip area and that high-slip patches are structurally bound by intersections or a change in strike. We note that the slip profiles from our simulated earthquakes have this characteristic (Figure 8), which lends some support for extrapolating rupture processes modeled at scales between 10^{-1} and 10^{2} m upward to larger faults. To the degree that our model represents an actual earthquake, then the high-slip region with greatest relief (Figure 4) might be an image of an asperity.

7. Conclusions

A numerical model taken directly from a measured natural fault surface can spontaneously generate stick-slip earthquake behavior. Initiation and termination of slip are controlled by stress heterogeneity that is in turn governed by changing contact geometry as slip evolves. Slip initiates in areas of strong surface gradients, where small displacements locally unclamp the fault. Slip terminates when multiple sticking points evolve where other steep gradient points collide (increased clamping stress). We show that the fault surface must change shape before slip can occur again and suggest that maturing faults must constantly change shape over time. Either these geometrical slip barriers smooth out as a fault system lengthens, leading to characteristic, larger-magnitude earthquakes, or self-similarity may lead to magnitude dependent segmentation. Post-rupture juxtaposition of new contacts and rupture barriers may make exact earthquake repeats rare except on very smooth faults.

Acknowledgments
We thank Chris Marone, an anonymous reviewer, and Editor Bob Nowack for their helpful comments and suggestions on this manuscript. Data are freely available from the authors.

References

Aki, K. (1987), Magnitude-frequency relation for small earthquakes: A clue to the origin of fmax of large earthquakes, *J. Geophys. Res.*, *92*, 1349–1355, doi:10.1029/JB092iB02p01349.

Aviles, C. A., C. H. Scholz, and J. Boatwright (1987), Fractal analysis applied to characteristic segments of the San Andreas fault, *J. Geophys. Res.*, *92*, 331–344, doi:10.1029/JB092iB01p00331.

Ben-David, O., and J. Fineberg (2011), Static friction coefficient is not a material constant, *Phys. Rev. Lett.*, *106*, 254301.

Bevk, A. (2013), Curbed SF. [Available at http://sf.curbed.com/archives/2013/08/12/rock_blasting_and_brick_making_atop_corona_heights_park.php.]

Brown, S. R., and C. H. Scholz (1985), Broad bandwidth study of the topography of natural rock surfaces, *J. Geophys. Res.*, *90*, 12,575–12,582, doi:10.1029/JB090iB14p12575.

Candela, T., F. Renard, J. Schmittbuhl, M. Bouchon, and E. E. Brodsky (2011), Fault slip distribution and fault roughness, *Geophys. J. Int.*, *187*, 959–968, doi:10.1111/j.1365-246X.2011.05189.x.

Candela, T., F. Renard, Y. Klinger, K. Mair, J. Schmittbuhl, and E. E. Brodsky (2012), Roughness of fault surfaces over nine decades of length scales, *J. Geophys. Res.*, *117*, B08409, doi:10.1029/2011JB009041.

Childs, C., T. Manzocchi, J. J. Walsh, C. G. Bonson, A. Nicol, and M. P. J. Schöpfer (2009), A geometric model of fault zone and fault rock thickness variations, *J. Struct. Geol.*, *31*(2), 117–127.

Collettini, C., A. Niemeijer, C. Viti, and C. Marone (2009), Fault zone fabric and fault weakness, *Nature*, *462*, 907–910.

Coon, E. T., B. E. Shaw, and M. Spiegelman (2011), A Nitsche-extended finite element method for earthquake rupture on complex fault systems, *Comput. Methods Appl. Mech. Eng.*, *200*(41–44), 2859–2870.

Dieterich, J. H. (1979), Modeling of rock friction: 1. Experimental results and constitutive equations, *J. Geophys. Res.*, *84*, 2161–2168, doi:10.1029/JB084iB05p02161.

Dieterich, J. H. (1992), Earthquake nucleation on faults with rate-and state-dependent strength, *Tectonophysics*, *211*, 115–134.

Duan, B., and D. D. Oglesby (2005), The dynamics of thrust and normal faults over multiple earthquake cycles: effects of dipping fault geometry, *Bull. Seismol. Soc. Am.*, *95*, 1623–1636, doi:10.1785/0120040234.
Faulkner, D. R., T. M. Mitchell, E. H. Rutter, and J. Cembrano (2008), On the structure and mechanical properties of large strike-slip faults, *Geol. Soc. Spec. Publ.*, *299*, 139–150.
Field, E. H., and M. T. Page (2011), Estimating earthquake-rupture rates on a fault or fault system, *Bull. Seismol. Soc. Am.*, *101*, 79–92, doi:10.1785/0120100004.
Field, E. H., et al. (2014), Uniform California Earthquake Rupture Forecast, Version 3 (UCERF3)—The time-independent model, *Bull. Seismol. Soc. Am.*, *104*, 1122–1180, doi:10.1785/0120130164.
Fournier, T., and J. Morgan (2012), Insights to slip behavior on rough faults using discrete element modeling, *Geophys. Res. Lett.*, *39*, L12304, doi:10.1029/2012GL051899.
Gudmundsson, A. (2004), Effects of Young's modulus on fault displacement, *C. R. Geosci.*, *336*, 85–92.
Imanishi, K., and W. L. Ellsworth (2006), Source scaling relationships of microearthquakes at Parkfield, CA, determined using the SAFOD pilot hole seismic array, in *Earthquakes: Radiated Energy and the Physics of Faulting*, edited by R. Abercrombie et al., AGU, Washington, D. C., doi:10.1029/170GM10.
Jennings, C. W. (1994), Fault activity map of California and adjacent areas with locations and ages of recent volcanic eruptions, California Division of Mines and Geology Data Map Series No. 6, 92 p., 2 plates, map scale 1:750,000.
Kagan, Y. Y. F. (1991), Dimension of brittle fracture, *J. Nonlinear Sci.*, *1*, 1–16.
Kezdi, A. (1974), *Handbook of Soil Mechanics*, 294 pp., Elsevier, Amsterdam.
Kirkpatrick, J. D., and E. E. Brodsky (2014), Slickenline orientations as a record of fault rock rheology, *Earth Planet. Sci. Lett.*, *408*, 24–34, doi:10.1016/j.epsl.2014.09.040.
Kirkpatrick, J. D., C. D. Rowe, J. C. White, and E. E. Brodsky (2013), Silica gel formation during fault slip: Evidence from the rock record, *Geology*, *41*, 1015–1018, doi:10.1130/G34483.1.
Lockner, D. A., and J. D. Byerlee (1993), How geometrical constraints contribute to the weakness of mature faults, *Nature*, *363*, 250–252.
Lynch, J. C., and M. A. Richards (2001), Finite element models of stress orientations in well-developed strike-slip fault zones: Implications for the distribution of lower crustal strain, *J. Geophys. Res.*, *106*, 26,707–26,729, doi:10.1029/2001JB000289.
Main, I. (1996), Statistical physics, seismogenesis, and seismic hazard, *Rev. Geophys.*, *34*, 433–462, doi:10.1029/96RG02808.
Manighetti, I., M. Campillo, C. Sammis, P. M. Mai, and G. King (2005), Evidence for self-similar, triangular slip distributions on earthquakes: Implications for earthquake and fault mechanics, *J. Geophys. Res.*, *110*, B05302, doi:10.1029/2004JB003174.
Marone, C. (1995), Fault zone strength and failure criteria, *Geophys. Res. Lett.*, *22*, 723–726, doi:10.1029/95GL00268.
Marone, C., and B. Kilgore (1993), Scaling of the critical slip distance for seismic faulting with shear strain in fault zones, *Nature*, *362*, 618–621.
Marone, C., M. Cocco, E. Richardson, and E. Tinti (2009), The critical slip distance for seismic and aseismic fault zones of finite width, *Int. Geophys.*, *94*(C), 135–162.
Moore, D. E., and M. J. Rymer (2007), Talc-bearing serpentinite and the creeping section of the San Andreas fault, *Nature*, *448*, 795–797.
Murchey, B. L., and D. L. Jones (1984), Age and significance of chert in the Franciscan Complex in the San Francisco Bay Region, in *Franciscan Geology of Northern California*, vol. 43, edited by M. C. Blake Jr., pp. 23–30, Pacific Section S.E.P.M.
Noda, H., E. M. Dunham, and J. R. Rice (2009), Earthquake ruptures with thermal weakening and the operation of major faults at low overall stress levels, *J. Geophys. Res.*, *114*, B07302, doi:10.1029/2008JB006143.
Okubo, P. G., and K. Aki (1987), Fractal geometry in the San Andreas fault system, *J. Geophys. Res.*, *92*, 345–355, doi:10.1029/JB092iB01p00345.
Page, M., and K. Felzer (2015), Southern San Andreas fault seismicity is consistent with the Gutenberg-Richter magnitude-frequency distribution, *Bull. Seismol. Soc. Am.*, *105*, doi:10.1785/0120140340.
Page, M. T., D. Alderson, and J. Doyle (2011), The magnitude distribution of earthquakes near Southern California faults, *J. Geophys. Res.*, *116*, B12309, doi:10.1029/2010JB007933.
Power, W. L., and T. E. Tullis (1992), The contact between opposing fault surfaces at Dixie Valley, Nevada, and implications for fault mechanics, *J. Geophys. Res.*, *97*, 15,425–15,435, doi:10.1029/92JB01059.
Power, W. L., T. E. Tullis, S. Brown, G. N. Boitnott, and C. H. Scholz (1987), Roughness of natural fault surfaces, *Geophys. Res. Lett.*, *14*, 29–32, doi:10.1029/GL014i001p00029.
Renard, F., T. Candela, and E. Bouchaud (2013), Constant dimensionality of fault roughness from the scale of micro-fractures to the scale of continents, *Geophys. Res. Lett.*, *40*, 83–87, doi:10.1029/2012GL054143.
Rice, J. R. (1992), Fault stress states, pore pressure distributions, and the weakness of the San Andreas Fault, in *Fault Mechanics and Transport Properties of Rocks; A Festschrift in Honor of W. F. Brace*, edited by B. Evans and T. Wong, pp. 475–503, Acad. Press, San Diego, Calif.
Ruina, A. (1983), Slip instability and state variable friction laws, *J. Geophys. Res.*, *88*, 10,359–10,370, doi:10.1029/JB088iB12p10359.
Sagy, A., E. E. Brodsky, and G. J. Axen (2007), Evolution of fault-surface roughness with slip, *Geology*, *35*, 283–286.
Schlocker, J. (1974), Geology of the San Francisco North quadrangle, California, *U.S. Geol. Surv. Prof. Pap.*, *782*, 109.
Scholz, C. H. (1987), Wear and gouge formation in brittle faulting, *Geology*, *15*, 493–495.
Scholz, C. H. (2002), *The Mechanics of Earthquake Faulting*, Cambridge Univ. Press, Cambridge, U. K.
Schwartz, D. P., and K. J. Coppersmith (1984), Fault behavior and characteristic earthquakes: examples from the Wasatch and San Andreas fault zones, *J. Geophys. Res.*, *89*, 5681–5698, doi:10.1029/JB089iB07p05681.
Sibson, R. H. (2003), Thickness of the seismic slip zone, *Bull. Seismol. Soc. Am.*, *93*, 1169–1178.
Stein, S., and A. Newman (2004), Characteristic and uncharacteristic earthquakes as possible artifacts: Applications to the New Madrid and Wabash seismic zones, *Seismol. Res. Lett.*, *75*, 173–187.
Toppozada, T. R., D. M. Branum, M. S. Reichle, and C. L. Hallstrom (2002), San Andreas fault zone, California: M ≥5.5 earthquake history, *Bull. Seismol. Soc. Am.*, *92*, 2555–2601.
Wells, D. L., and K. J. Coppersmith (1994), New empirical relationships among magnitude, rupture length, rupture width, rupture area, and surface displacement, *Bull. Seismol. Soc. Am.*, *84*, 974–1002.
Wesnousky, S. G. (1994), The Gutenberg-Richter or characteristic earthquake distribution, which is it?, *Bull. Seismol. Soc. Am.*, *84*, 1940–1959.
Wesnousky, S. G. (2006), Predicting the endpoints of earthquake ruptures, *Nature*, *444*, 358–360.
Wibberley, C. A. J., G. Yielding, and G. Di Toro (2008), Recent advances in the understanding of fault zone internal structure: A review, *Geol. Soc. Spec. Publ.*, *299*, 5–33.
Xing, H. L., P. Mora, and A. Makinouchi (2004), Finite element analysis of fault bend influence on stick–slip instability along an intra-plate fault, *Pure Appl. Geophys.*, *161*, 2091–2102, doi:10.1007/s00024-004-2550-1.
Xu, S., E. Fukuyama, Y. Ben-Zion, and J.-P. Ampuero (2015), Dynamic rupture activation of backthrust fault branching, *Tectonophysics*, *644–645*, 161–183.